STATIC PERFORMANCE AND DESIGN OF COLD-FORMED HIGH STRENGTH STEEL RECTANGULAR HOLLOW SECTION X-JOINTS

Madhup Pandey* and Ben Young

Department of Civil and Environmental Engineering, The Hong Kong Polytechnic University, Hong Kong, China

Abstract

Cold-formed high strength steel (CFHSS) X-joints made of square and rectangular hollow sections (SHS and RHS) brace and chord members were investigated in this study. The steel grades of tubular members were S900 and S960 with the nominal 0.2% proof stresses of 900 and 960 MPa, respectively. The authors carried out tests on cold-formed S900 and S960 steel grades RHS X-joints. The test results were used to develop accurate finite element (FE) models in this study. Using the validated FE models, a comprehensive FE parametric study was then performed. The validity ranges of critical geometric parameters were extended beyond the current limits mentioned in international codes and guides. The nominal resistances predicted from existing design rules given in European code and *Comité International pour le Développement et l´Etude de la Construction Tubulaire* (CIDECT) were compared with a total of 726 test and FE joint resistances, including 684 numerical data generated in this study. Chord face failure, chord side wall failure and a combination of these two failure modes were reported. It is shown that design rules given in European code and CIDECT are not suitable for the range of cold-formed S900 and S960 steel grades RHS X-joints investigated in this study. Therefore, user-friendly, accurate and reliable design equations are proposed in this study. Moreover, reliability analysis was also performed for the existing and proposed design equations.

Keywords: Cold-formed steel; Design equations; FE analysis; High strength steel; S900 and S960 steels; Tubular joints; X-joints.

---

*Corresponding author (e-mail: madhup.pandey@polyu.edu.hk)

1. Introduction

Hollow section members are prominently used as primary loading carrying structural elements due to the excellent amalgamation of their aesthetical, architectural and structural features. More importantly, these merits are complimented by easy jointing possibilities when square and rectangular hollow sections (SHS and RHS) are used as the chord members. High strength steel (HSS) (i.e. steel grade higher than S460) hollow section members are in high demand in various civil engineering projects because of their superior strength per unit weight and reduced handling costs. However, the lack of adequate research work hampers their practical applications. Nonetheless, certain investigations on the structural performance of HSS open section members [1,2], tubular members [3,4], built-up box section joints [5-7], and cold-formed steel (CFS) tubular joints [8-17] have been conducted in recent years. HSS is commonly produced by two methods, namely by adding alloying elements and by heat treatment method. In HSS, strengthening the ferrite by grain refining, precipitation strengthening, and solid-solution strengthening is the main purpose of alloying elements (Cu, Ni, Mn, Cr and Mo) [18]. While grain refinement and precipitation strengthening depend on the intricate interactions between alloy design and thermo-mechanical treatment, solid-solution strengthening is mainly related to alloy contents. In order to lower the temperature at which austenite transforms into ferrite and pearlite during air cooling, alloying elements are also chosen to affect transformation temperatures. This reduction in transformation temperature results in a product with a finer grain, which is a significant source of strengthening. On the other hand, popular heat treatment methods for carbon steel include quenching and tempering (QT) and thermo-mechanical controlled processing (TMCP). The QT method provides tempered martensitic or bainitic microstructure that results in remarkable comprehensive mechanical properties, including very high strength and good toughness for both low and medium carbon steels [19,20]. However, TMCP is a microstructural control technique combining controlled rolling and cooling. The main objective of the TMCP method is to replace the ferrite/pearlite banding structure of traditional steels with a fine and uniform acicular ferrite microstructure. The increased strength and superior toughness of TMCP steels are attributed to the presence of fine and homogenous acicular ferrite microstructure [21].

Currently, the majority of international codes [22-24] and guides [25,26] restrict the use of design rules of tubular joints up to S460 steel grade. However, EC3 [27] permits the design of tubular joints with steel grades up to S700. It is worth noting that the experimental, analytical and numerical studies conducted on S355 and lower steel grades tubular joints formed the basis of design rules given in codes [22-24,27] and guides [25,26]. The design rules first developed for mild steel grades are now extended up to S700 steel grade by duly multiplying the existing design rules with a material factor (C_f). As a result, the suitability of current design rules remains questionable for steel grades higher than S700, which in turn formed the basis of the investigation presented in this paper. A comprehensive numerical investigation and design of cold-formed S900 and S960 steel grades SHS and RHS (henceforth, RHS includes SHS) X-joints are presented in this paper. Literature review has confirmed that, at present, no other research is available on CFS X-joints of steel grades exceeding S700, except for the experimental investigations carried out by Pandey and Young [28,29]. Using the test results [28,29], accurate finite element (FE) models were developed in this investigation. A thorough parametric study was then carried out using the verified FE models. The predictions from EC3 [24] and CIDECT [26] were compared with the ultimate capacities (N_f) of test and FE specimens. The current design rules have been demonstrated to be unsuitable for the range of RHS X-joints investigated in this study. Therefore, accurate and reliable design equations are proposed in this study to predict the N_f of CFS S900 and S960 steel grades RHS X-joints.

2. Outline of experimental investigations

In the experimental investigations [28,29], braces and chords of cold-formed high strength steel (CFHSS) X-joints were made of RHS members. The braces and chords were welded using fully robotic metal active gas welding. In total, 42 tests were carried out by Pandey and Young [28,29], where test specimens were axially compressed via braces. The angles between brace and chord members (θ_1) were 30°, 50°, 70° and 90°. The nominal 0.2% proof stresses of RHS members were 900 and 960 MPa. Fig. 1 presents various notations for RHS X-joint. The static behaviour of RHS X-joint primarily depends on non-dimensional geometric ratios, including β (b_1/b_0), τ (t_1/t_0), 2γ (b_0/t_0) and h_0/t_0. The symbols b, h, t and R stand for cross-section width, depth, thickness and external corner radius of RHS member, respectively. The subscripts 0 and 1 denote chord and brace, respectively. In the experimental investigations, β ranged from 0.34 to 1.0, τ ranged from 0.52 to 1.28, 2γ ranged from 20.2 to 38.9, and h_0/t_0 ranged from 12.7 to 39.0. Pandey and Young [30,31] detailed the material properties of RHS members and welding filler material used in the tests of CFHSS X-joints [28,29]. The measured static yield strengths of tubular members ranged from 910 to 1059 MPa, while the measured static yield strength of welding filler material was 965 MPa. The failure modes identified in the tests were chord face failure (F), chord side wall failure (S) and a combination of these two failure modes, named combined failure (F+S). In order to avoid the influence of loading rate from the test results, the tests were paused for 2 minutes near the ultimate and in the post-ultimate regions, which has also been used in other studies [8-12,32]. The test results were obtained in the form of static N vs u and N vs v curves, where N, u and v respectively stand for static load, chord face indentation and chord side wall deformation.

3. Numerical program

3.1. Development of FE models

3.1.1. Introduction

ABAQUS [33] was used to perform the comprehensive numerical investigation. The isotropic strain hardening law was selected for FE analyses. The yielding onsets of FE specimens were based on the von-Mises yield theory. In the FE analyses, the growth of the time step was kept non-linear in order to reduce the overall computation time. Furthermore, the default Newton-Raphson method was used to find the roots of non-linear equilibrium equations. The material non-linearity was considered by assigning the measured values of static stress-strain curves of different regions of the tubular member in the plastic material definition part of the FE models. On the other hand, the geometric non-linearities in FE models were considered by enabling the non-linear geometry parameter (*NLGEOM) in ABAQUS [33]. Furthermore, various parameters, including through-thickness division, contact interactions, mesh seed spacing, corner region extension and element types, were also studied and reported in the following sub-sections of this paper. Fig. 2 presents typical FE X-joint specimens modelled in this study.

3.1.2. Meshing, element type and material properties

Except for the welds, all other parts of FE models were developed using C3D20 elements. On the other hand, C3D10 element was used to model the weld parts due to their complicated shapes. The use of solid elements helped in making realistic fusions between tubular and weld parts of FE models. Convergence studies were conducted using different mesh sizes, and finally, chord and brace members were seeded at 4 mm and 7 mm intervals, respectively. Moreover, the seeding intervals of weld parts reciprocated the seeding spacings of their respective brace parts. In order to assure the smooth transfer of stresses from flange to web regions, the corner portions of RHS were split into ten elements. FE analyses were also conducted to examine the influence of divisions along the wall thickness (t) of tubular members. The results of these FE analyses demonstrated the trivial influence of wall thickness divisions on the load vs deformation curves of the investigated RHS X-joints. The use of the C3D20 element as well as the small thickness of test specimens [28,29] lead to such observations. It is worth noting that similar findings were also obtained in other studies [34-36]. Thus, for the validation of FE models, the wall thickness of tubular members was not divided. The test specimens in the experimental programs [28,29] were fabricated from tubular members that belonged to the same batch of tubes used in other investigations conducted by Pandey and Young [8-12,30,31]. On the other hand, Pandey and Young [22] investigated the material properties of welding filler material. The true stress-strain curves of flat and corner portions of RHS members and welding filler material were allocated to the corresponding parts of the FE specimens. In this study, the influence of cold-working was included in FE models by assigning wider corner regions. Various distances for corner extension were considered in the sensitivity analyses, and finally, the corner portions were extended by $2t$ into the neighbouring flat portions, which was in agreement with other studies conducted on CFHSS tubular members and joints [35-38].

3.1.3. Weld modelling and contact interactions

Welds were modelled in all FE models using the average values of measured weld dimensions [28,29]. The fillet weld was modelled for FE specimens when $\beta \leq 0.80$. However, when $\beta > 0.80$, groove and fillet welds (GW and FW) were respectively modelled along the length and width of the chords. The inclusion of weld geometries and weld material properties considerably improved the overall accuracies of FE models. Two types of interactions were defined in FE models, first, brace-chord interaction, and second, weld-tubular member interaction. Both these types of interactions were established using the built-in surface-to-surface contact definition. The interactions were kept frictionless, and along the normal direction, 'hard' contact pressure overclosure was used. In addition, finite sliding was permitted between the interaction surfaces. The interaction surfaces between brace-chord members as well as weld-tubular members were connected to each other using the 'master-slave' algorithm technique. This technique permits the separation of fused surfaces under tension, however, it does not allow penetration of fused surfaces under compression.

3.1.4. Load application

The boundary conditions were set at the reference points by constraining the displacements [39]. The top and bottom reference points (TRP and BRP) were created at the cross-section centre of brace members, as shown in Fig. 2. Subsequently, TRP and BRP were coupled to their respective brace end cross-section surfaces using kinematic coupling type. In order to exactly replicate the test setup, all degrees of freedom (DOF) of TRP were restrained. On the other hand, except for translation along the height of the specimen, all other DOF of BRP were also restrained. Moreover, all DOF of other nodes of FE specimen were kept unrestrained for rotation and translation. Using the displacement control method, compression load was then applied at the BRP of FE models. Following this approach, the boundary conditions and load application in FE analyses were identical to those used in the test programs [28,29].

3.1.5. Weld heat affected region (WHAR)

The design recommendations in international codes and guides [22-27] are identical for HSS produced by different methods. However, it has been reported in some recent studies [29,40-43] that HSS produced by different methods exhibited different extents of softening around the welds. Investigations carried out by Stroetmann et al. [40], Javidan et al. [41] and Amraei et al. [42,43] reported 16% to 32% reductions in the ultimate strengths of S960 steel grade parent materials around the welds. Fig. 3(a) presents the definition of weld heat affected region (WHAR) proposed by Pandey et al. [35]. The material properties of WHAR of S960 steel grade RHS members with thicknesses ranging from 3 to 6 mm were investigated by Pandey and Young [29]. A 14% to 32% reduction in the ultimate strengths of the parent metals was reported in the first 6 mm distance of the heat affected region [29]. It should be stressed that the RHS members used in Pandey and Young [29] were taken from the same batch of tubes as those used in other investigations [8-12,28,29,35,36]. A strength reduction (S_{rl}) model was proposed by Pandey et al. [35] for S900 and S960 steel grades tubular joints to integrate the material properties of WHAR in FE models, as illustrated in Fig. 3(b). On the other hand, Fig. 4 presents the spread of WHAR for typical RHS X-joints. The proposed strength reduction model was successfully used to perform the numerical investigation and design of CFHSS T- and TF-joints [35,36]. Therefore, it was also included in this investigation, and accordingly, material properties were assigned to the WHAR of all RHS X-joint FE specimens. The adoption of WHAR remarkably improved the accuracies of FE models, and thus, the numerical results. In this study, the ignorance of WHAR over-estimated the joint resistances of cold-formed S900 and S960 steel grades RHS X-joints failed by chord face failure, combined failure and chord side wall failure in the range of 4% to 9%, 6% to 16% and 3% to 61%, respectively.

3.1.6. Geometric imperfection in chord webs of equal-width RHS X-joints

Garifullin et al. [44] studied the influence of geometric imperfections on the behaviour of hollow section joints. The BUCKLE command of ABAQUS [44] was used to implement this methodology. The first mode of the elastic buckling analysis of a FE specimen was treated as the imperfection mode of that specimen. The deformation scale of the first buckling mode was then ramped up to match the EN [45] limits. The scaled eigenmode shape was then superimposed on the FE model. Garifullin et al. [44] concluded the trivial influence of geometric imperfections on the static behaviour of hollow section joints. However, Pandey et al. [35] reported that the maximum measured values of cross-section width and depth of RHS members were on an average 2.9% more than their respective nominal dimensions. As tubular members used to fabricate RHS X-joints in tests [28,29] belonged to the same batch of tubes used in Pandey et al. [35], thus, it was necessary to model this geometric imperfection as an outward bulging 3-point convex arc, as shown in Fig. 5. As all failure modes in tests [30,31] and numerical investigations [35,36] were only governed by the deformation of chord members, Pandey et al. [35] numerically examined the influence of outward bulging of chord cross-section on the static behaviour of hollow section joints. Finally, Pandey et al. [35] concluded that the effect of convex outward bulging of chord cross-section was significant only for equal-width (i.e. β=1.0) RHS joints. As a result, in this investigation, geometric imperfections were introduced as a 3-point convex arc in the chord webs of equal-width RHS X-joints.

3.2. Validation of FE models

The FE models of cold-formed S900 and S960 steel grades RHS X-joints were developed using the modelling approaches described in the preceding section of this paper. The test results of RHS X-joints reported in Pandey and Young [28,29] were used to validate the FE model. The validation was performed by duly comparing the ultimate capacities, load-deformation histories and failure modes between test and FE specimens. The measured dimensions of tubular members and welds were used to develop all FE models. In addition, measured material properties of tubular members, welds and WHAR were also included. The ultimate capacities (N_f) of X- and non-90° X-joints test specimens were compared with those predicted from their corresponding FE models (N_{FE}) in Tables 1 and 2, respectively. The values of mean (P_m) and coefficients of variation (COV) (V_p) of the comparisons for 90° X-joints are 1.01 and 0.016, respectively. On the other hand, the values of mean and COV of the comparisons for non-90° X-joints are 1.01 and 0.021, respectively. It is worth mentioning that both ultimate load and 3% deformation limit load were used to determine the N_f of test and FE specimens. In addition, Figs. 6 and 7 present the comparisons of load vs deformation curves for typical X- and non-90° X-joints test and FE specimens, respectively. Moreover, the comparisons of failure modes between typical X- and non-90° X-joints test and FE specimens are shown in Figs. 8 and 9, respectively. Thus, the validated FE models closely replicated the overall static behaviour of cold-formed S900 and S960 steel grades RHS X-joints, as shown in Tables 1-2 and Figs. 6-9.

3.3. Parametric study

3.3.1. FE modelling specifications

In total, 684 FE analyses were performed in the parametric study. The parametric FE specimens were designed such that θ_1 ranged from 30° to 90°, β ranged from 0.30 to 1.0, 2γ ranged from 16.6 to 50, h_0/t_0 ranged from 10 to 60, η ranged from 0.3 to 1.2, and τ ranged from 0.75 to 1.0. Overall, the values of cross-section width and depth of braces and chords of parametric FE specimens ranged from 30 mm to 600 mm, while the wall thickness of braces and chords ranged from 2.25 mm to 10 mm. The external corner radii of braces and chords (R_1 and R_0) conformed to commercially produced HSS members [46,47]. In this study, R_1 and R_0 were kept as $2t$ for $t \leq 6$ mm, $2.5t$ for $6 < t \leq 10$ mm and $3t$ for $t > 10$ mm, which in turn also met the limits detailed in EN [45]. For 90° RHS X-joints, brace and chord lengths (L_1 and L_0) were designed as $2\times\max[b_1,h_1]$ and $4h_0+h_1$, respectively. On the other hand, for non-90° X-joints, the brace length from the heel location (L_H) was designed as $2\times\max[b_1,h_1]$, while the chord length (L_0) was kept as $3h_0 + h_0 \tan(90-\theta_1) + h_1/\cos(90-\theta_1)$. For meshing along the longitudinal and transverse directions of tubular members, seedings were approximately spaced at the minimum of $b/30$ and $h/30$. Overall, the adopted mesh sizes of parametric FE specimens ranged from 3 mm to 12 mm. On the other hand, the seeding interval of weld parts of parametric FE specimens reciprocated the seeding interval of their corresponding brace parts. For RHS members with $t \leq 6$ mm, no divisions were made along the wall thickness of parametric FE specimens. However, for RHS members with $t > 6$ mm, the wall thickness of parametric FE specimens was divided into two layers. The parametric study used all FE modelling techniques described earlier in the paper.

Following the prequalified tubular joint details given in AWS [48], the leg size (w) of FW in 90° X-joints was designed as 1.5 times the minimum of t_1 and t_0. On the other hand, for non-90° X-joints, the welds around the joint perimeter were designed by duly keeping the weld leg length equal to 2.5 times the minimum of t_1 and t_0, which made the throat thickness equal to $1.77t$. This design approach satisfied the requirements given in both AWS [48] and CIDECT [26]. The static material properties of flat and corner portions of RHS 150×150×6 [30] were assigned to the corresponding portions of all tubular members of parametric FE specimens. Besides, weld parts of all parametric

FE specimens were given the measured material properties of welding filler material [31]. For RHS 150×150×6, the measured static values of 0.2% proof stress, ultimate stress, fracture strain and Ramberg-Osgood parameter were 1059 MPa, 1146 MPa, 9.4% and 5.3, respectively [30]. On the other hand, for the weld material, the measured static values of 0.2% proof stress, ultimate stress, fracture strain and Ramberg-Osgood parameter were 965 MPa, 1023 MPa, 17.2% and 8.1, respectively [31]. Moreover, the material properties and spread of WHAR were assigned in accordance with the recommendations proposed by Pandey et al. [35]. Additionally, the flat parts of chord webs (i.e. h_0-2R_0) of all equal-width 90° and non-90° X-joints were modelled as an outward bulging 3-point arc. The flat part of each chord web was outward bulged at its centre by 0.015b_0, thus, the maximum chord width ($b_{0,max}$) of 90° and non-90° X-joints with β=1.0 at the centre of the chord webs was 1.03b_0, as shown in Fig. 5.

3.3.2. Failure modes

Three types of failure modes were identified in the experimental [28,29] and numerical investigations. First, failure of X-joints by chord flange yielding, which was named as chord face failure and denoted by the letter 'F' in this study. Second, failure of X-joints due to buckling of chord webs, which was termed as chord side wall failure and denoted by the letter 'S' in this study. Third, failure of X-joints due to a combination of chord face and chord side wall failures, which was called as the combined failure and denoted by 'F+S' in this study. It is important to note that these failure modes were defined corresponding to the N_f, which in turn was computed by combinedly considering the ultimate and 0.03b_0 limit loads, whichever occurred earlier in the N vs u curve [26]. The same approach was used to determine the N_f in test programs [28,29]. The test and parametric FE specimens were failed by the F mode, when N_f was predominantly determined using the 0.03b_0 limit. The applied loads of X-joints failed by the F mode were monotonically increasing. The test and parametric FE specimens were failed by the F mode in this investigation when $0.30 \leq \beta \leq 0.75$. On the other hand, in this study, test and parametric FE specimens were failed by the S mode when β=1.0. The load vs deformation curves of test and parametric FE specimens that failed by the F+S mode exhibited a clear ultimate load. Additionally, test and parametric FE specimens that failed by the F+S mode showed evident deformations of chord flange, chord webs and chord corner regions. The specimens were failed by the F+S mode in this investigation when $0.80 \le \beta \le 0.90$. Moreover, none of the test and FE specimens were failed by the global buckling of braces.

4. Existing design provisions

In order to examine the suitability of design rules given in EC3 [24] and CIDECT [26] for CFHSS RHS X-joints, the N_f of test and parametric FE specimens were evaluated against the nominal resistances ($N_{E,X}^{*}$, $N_{E,X}$, $N_{C,X}^{*}$ and $N_{C,X}$) predicted from these specifications [24,26,27]. The measured dimensions and properties were used to calculate the nominal resistances. The symbols $N_{E,X}^{*}$ and $N_{C,X}^{*}$ stand for nominal resistances predicted from EC3 [24] and CIDECT [26] without including the recommended material factors. On the contrary, the symbols $N_{E,X}$ and $N_{C,X}$ stand for nominal resistances predicted from EC3 [24] and CIDECT [26] by duly including the recommended material factors. The $N_f / N_{E,X}$ and $N_f / N_{C,X}$ ratios checked the applicability of the current design rules. However, the $N_f / N_{E,X}^{*}$ and $N_f / N_{C,X}^{*}$ ratios checked the applicability of design rules developed for mild steel RHS X-joints.

Chord face plastification failure (*$\beta \le 0.85$*)

EC3 [24]:

For steel grades up to S355 or below:

$$N_{E,X}^{*} = \frac{k_n f_{y0} t_0^2}{(1-\beta)\sin\theta_1}\left(\frac{2\eta}{\sin\theta_1} + 4\sqrt{1-\beta}\right) / \gamma_{M5} \tag{1}$$

For steel grades higher than S355:

$$N_{E,X} = C_f \left(N_{E,X}^{*}\right) \tag{2}$$

CIDECT [26]:

For steel grades up to S355 or below:

$$N_{C,X}^{*} = Q_f \frac{f_{y0} t_0^2}{\sin\theta_1}\left(\frac{2\eta}{(1-\beta)\sin\theta_1} + \frac{4}{\sqrt{1-\beta}}\right) \tag{3}$$

For steel grades higher than S355:

$$N_{C,X} = C_f\left(N^*_{C,X}\right) \tag{4}$$

Chord side wall buckling failure ($\beta = 1.0$)

EC3 [24]:

For steel grades up to S355 or below:

$$N^*_{E,X} = k_n \frac{f_b t_0}{\sin\theta_1}\left(\frac{2h_1}{\sin\theta_1} + 10t_0\right) / \gamma_{M5} \tag{5}$$

For steel grades higher than S355:

$$N_{E,X} = C_f\left(N^*_{E,X}\right) \tag{6}$$

CIDECT [26]:

For steel grades up to S355 or below:

$$N^*_{C,X} = Q_f \frac{f_k t_0}{\sin\theta_1}\left(\frac{2h_1}{\sin\theta_1} + 10t_0\right) \tag{7}$$

For steel grades higher than S355:

$$N_{C,X} = C_f\left(N^*_{C,X}\right) \tag{8}$$

The nominal resistances from EC3 [24] were obtained using 0.2% proof stress and partial safety factor (γ_{M5}) equal to 1.0. On the contrary, CIDECT [26] uses the minimum of yield stress and 0.80 times the respective ultimate stress for joint resistance calculation. Unlike EC3 [24], CIDECT [26] uses different values of partial safety factors (γ_M) for different tubular joints, which are given in IIW [25]. However, their effects are implicitly included in the design rules given in CIDECT [26]. In this study, the nominal resistances from CIDECT [26] were calculated using γ_M equal to 1.0 and 1.25 for the F and S modes, respectively. In Eqs. (1) to (8), chord stress functions are denoted by k_n and Q_f (in this investigation, the values of k_n and Q_f were adopted as 1.0), the yield stress of chord member is denoted by f_{y0}, η is equal to h_1/b_0, chord side wall buckling stresses are denoted by f_b and f_k, and angle between brace and chord (θ_1) is in degrees.

In addition, a reliability analysis was performed as per AISI S100 [49]. In this study, the design equation was treated as reliable when the value of the reliability index (β_0) was greater than or equal to 2.50. The values of various statistical parameters and load combinations used in the reliability index calculation are identical to those values adopted in Pandey et al. [35].

5. Comparisons of ultimate capacities with nominal resistances

The comparison summary of N_f with nominal resistances predicted from design rules given in EC3 [24] and CIDECT [26] are shown in Tables 3-5. In total, 726 data are summarised in Tables 3-5, including 42 test data [28,29] and 684 parametric FE data generated in this study. The comparisons are also graphically shown in Figs. 10-12. In Fig. 10, generally, test and parametric FE specimens with small values of β and η ratios and large values of 2γ ratio lie below the unit slope line (i.e. y=x). For such specimens, the joint resistance corresponding to the $0.03b_0$ limit was insufficient to cause the yielding of chord connecting flanges. On the other hand, the yield line theory was used to derive the existing design equation for specimens that failed by the F mode [24,26]. Hence, N_f of test and parametric FE specimens became smaller than the corresponding nominal resistances predicted from EC3 [24] and CIDECT [26]. As a result, such data fall below the line of unit slope. The data above the line of unit slope, on the other hand, indicate test and parametric FE specimens with medium to large values of β and η ratios and small values of 2γ ratio. In Fig. 11, the data above the line of unit slope typically represent test and parametric FE specimens with large values of β ratio and small values of 2γ and h_0/t_0 ratios. As the β ratio of test and parametric FE specimens failed by the F+S mode increased, the brace member gradually approached the chord corner regions. Consequently, N_f of such joints increased because of enhanced rigidity of corner regions. On the other hand, the corresponding increase in nominal resistances predicted from specifications [24,26,27] was lower than the N_f of test and parametric FE specimens. Subsequently, such data fall above the line of unit slope in Fig. 11. The comparison results of the test and parametric FE specimens that failed by the S mode are shown in Fig. 12. The existing design rule apparently provided very conservative predictions and was accompanied by very large values of COV. The current design rule given in EC3 [24] and CIDECT [26] for the S failure mode considered chord webs as pin-ended columns, resulting in very conservative predictions. The extent of conservatism sharply increased with the increase of h_0/t_0 and the decrease of θ_1.

6. Proposed design rules

User-friendly, accurate and reliable design rules are proposed in this study for different identified failure modes. The design rules are proposed for S900 and S960 steel grades tubular members produced via TMCP method. Cai et al. [50] reported that the strength deteriorations in the hardened and softened heat affected zones are higher in TMCP high strength steel compared to QT high strength steel. Therefore, the design rules proposed in this study can also be conservatively used for cold-formed S900 and S960 steel grades RHS X-joints produced via QT method. As welds were modelled in all parametric FE specimens, the influences of weld and associated WHAR were implicitly included in the proposed design rules. In order to obtain design resistances (N_d), the proposed nominal resistances (N_{pn}) in the following sub-sections of this paper shall be multiplied by their correspondingly recommended resistance factors (ϕ), i.e. $N_d = \phi\ (N_{pn})$.

6.1. Chord face failure (F) mode ($0.30 \le \beta \le 0.75$)

By taking into consideration the effect of important geometric factors as well as the P_m and V_p of the overall comparison, a design equation (Eq. (9)) is proposed to predict the nominal resistance of cold-formed S900 and S960 steel grades RHS X-joint failed by the F mode.

$$N_{pn} = \frac{f_{y0} t_0^2}{(\sin\theta_1)^{1.4}} \left[\frac{28\beta + 7\eta - 7}{1 + 0.01(2\gamma)} \right] \tag{9}$$

The Eq. (9) is valid for $\theta_1 \ge 30°$, $0.30 \le \beta \le 0.75$, $16.6 \le 2\gamma \le 50$, $15 \le h_0/t_0 \le 50$, $0.3 \le \eta \le 1.2$ and $0.67 \le \tau \le 1.33$. Eq. (9) must be multiplied by ϕ equal to 0.75 to obtain the design resistance (N_d). The comparisons of test and FE resistances vs nominal and proposed resistances are graphically presented in Fig. 10. The summary of comparison results is detailed in Table 3.

6.2. Combined failure (F+S) mode ($0.80 \le \beta \le 0.90$)

In order to predict the nominal resistance of cold-formed S900 and S960 steel grades RHS X-joint failed by the F+S mode, a design equation (Eq. (10)) is proposed by taking into consideration the effect of important geometric factors as well as the P_m and V_p of the overall comparison.

$$N_{pn} = \frac{f_{y0} t_0^2}{(\sin\theta_1)^{(0.04\theta_1 - 0.1)}} \left[\frac{60\beta + 8\eta - 38}{0.9 + 0.003(2\gamma)} \right] \tag{10}$$

The Eq. (10) is valid for $\theta_1 \ge 30°$, $0.80 \le \beta \le 0.90$, $16.6 \le 2\gamma \le 50$, $12.5 \le h_0/t_0 \le 50$, $0.5 \le \eta \le$

1.2 and $0.5 \leq \tau \leq 1$. Eq. (10) must be multiplied by ϕ equal to 0.70 to obtain the design resistance (N_d). The comparisons of test and FE resistances vs nominal and proposed resistances are graphically presented in Fig. 11. The summary of comparison results is detailed in Table 4.

6.3. Chord side wall failure (S) mode ($\beta = 1.0$)

The gross conservatism of the current chord side wall failure design rule given in EC3 [24] and CIDECT [26] is a widely known issue. It has been well acknowledged and reported in many studies [14,28-31,35,36,51-58]. In this study, two design equations (Eqs. (11) and (13)) are proposed for specimens that failed by the S mode (N_{pn1} and N_{pn2}). The design equation in the first proposal (i.e. Eq. (11)) is formulated by duly taking into consideration the effect of important geometric factors as well as the P_m and V_p of the overall comparison.

$$N_{pn1} = \frac{f_k\left(2b_w t_0\right)}{\left(\sin\theta_1\right)^{0.7}\left(0.4\eta+2\right)}\left[\frac{1.4-0.05\left(2\gamma\right)+2.4\tau}{2e^{\mathrm{H}}}\right] \tag{11}$$

where

$$\mathrm{H} = -0.05\left(\frac{h_0}{t_0}\right)^{\left(1.1-\frac{\theta_1}{1000}\right)} \tag{12}$$

The Eq. (11) is valid for $\theta_1 \geq 30°$, $\beta = 1.0$, $16.6 \leq 2\gamma \leq 40$, $10 \leq h_0/t_0 \leq 60$, $0.5 \leq \eta \leq 1.2$ and $0.75 \leq \tau \leq 1.33$. The buckling curve 'a' of EC3 [59] was used to determine f_k in Eq. (11). In this study, the effective lengths of the flat portions of chord side walls were taken as $0.85\times(h_0\text{-}2R_0)$. The definition of the width of chord web column (b_w) was identical to that given in EC3 [24] and CIDECT [26].

The design rule (i.e. Eq. (13)) in the second proposal is formulated by modifying the design equation proposed by Lan et al. [51]. One of the modifications included a revised buckling reduction factor (χ) for RHS X-joints investigated in this study, as shown in Eq. (15). In addition, as the influence of θ_1 on the ultimate capacities of RHS X-joints was thoroughly investigated in this study, a more precise expression was used to consider the effect of θ_1 in Eq. (13).

$$N_{pn2} = \frac{C_f f_k t_0\left(2h_1+10t_0\right)}{\left(\sin\theta_1\right)^{0.7}} \tag{13}$$

$$f_k = \chi\left(\frac{h_0}{h_1}\right)^{0.15} f_{y0} \leq f_{y0} \tag{14}$$

where $$\chi = 1.15 - 0.1\left(\frac{h_0}{t_0}\right)^{0.3}\sqrt{\frac{f_{y0}}{355}} \leq 1.0 \tag{15}$$

Eqs. (11) and (13) must be multiplied with ϕ equal to 0.70 and 0.75, respectively, to obtain the corresponding design resistances (N_d). The comparisons of test and FE resistances vs nominal and proposed resistances are graphically presented in Fig. 12. The summary of comparison results is shown in Table 5.

It is important to note that linear interpolation is required between Eqs. (9)-(10) and Eqs. (10)-(11) to obtain the nominal resistances of cold-formed S900 and S960 steel grades RHS X-joints with $0.75 < \beta < 0.80$ and $0.90 < \beta < 1.0$, respectively.

6.4. Unified design equations

The design equations to predict the ultimate capacities of cold-formed S900 and S960 steel grades simply supported T-joints and fully chord supported T-joints (denoted by TF-joints) are proposed by Pandey et al. [35,36]. In order to propose unified design equations, an attempt has been made to keep the format of the proposed design equations matching between X-, T- and TF-joints failed by identical failure modes. The unified design equations for different failure modes are proposed as follows:

- For cold-formed S900 and S960 steel grades X-, T- and TF-joints failed by F mode ($0.30 \leq \beta \leq 0.75$) and F+S mode ($0.80 \leq \beta \leq 0.90$):

$$N_{pn} = \frac{f_{y0}t_0^2}{(\sin\theta_1)^{\mathrm{F}}}\left[\frac{\mathrm{A}\beta + \mathrm{B}\eta + \mathrm{C}}{\mathrm{D} + \mathrm{E}(2\gamma)}\right] \tag{16}$$

- For cold-formed S900 and S960 steel grades X-, T- and TF-joints failed by S mode ($\beta = 1.0$):

$$N_{pn} = \frac{f_k(2b_w t_0)}{(\sin\theta_1)^{\mathrm{G}}(\mathrm{E}\eta + \mathrm{F})}\left[\frac{\mathrm{A} + \mathrm{B}(2\gamma) + \mathrm{C}\tau}{\mathrm{D}}\right] \tag{17}$$

The values of coefficients (A to G) used in Eqs. (16) and (17) are given in Tables 6 to 8 for F, F+S and S modes, respectively. It should be noted that linear interpolation is required to predict the nominal resistances of the investigated RHS X-joints with $0.75 < \beta < 0.80$ and $0.90 < \beta < 1.0$.

7. Conclusions

The main concluding remarks drawn from this study are as follows:

- The modelling of weld parts and inclusion of WHAR significantly improved the overall accuracy of the finite element models developed using second-order solid elements.
- The investigated RHS X-joints were failed by chord face failure (F), chord side wall failure (S), and a combination of these two failure modes, i.e. combined failure mode (F+S).
- The current design rules given in EC3 [24] and CIDECT [26] are found unsuitable for the range of tests [28,29] and parametric FE specimens investigated in this study.
- Accurate, less dispersed, user-friendly and reliable design equations are proposed for cold-formed S900 and S960 steel grades RHS X-joints.
- Unified design equations are also proposed to predict the nominal resistances of cold-formed S900 and S960 steel grades RHS X-, T-, TF-joints failed by F, S and F+S modes.

Acknowledgement

The work described in this paper was fully supported by a grant from the Research Grants Council of the Hong Kong Special Administrative Region, China (Project No. 17210218).

References

[1] Wang F, Zhao O and Young B. Testing and numerical modelling of S960 ultra-high strength steel angle and channel section stub columns. Engineering Structures 2020;204:109902.

[2] Wang F, Zhao O and Young B. Flexural behaviour and strengths of press-braked S960 ultra-high strength steel channel section beams. Engineering Structures 2019;200:109735.

[3] Ma JL, Chan TM and Young B. Design of cold-formed high strength steel tubular beams. Engineering Structures 2017; 151:432-443.

[4] Ma JL, Chan TM and Young B. Cold-formed high-strength steel rectangular and square hollow sections under combined compression and bending. Journal of Structural Engineering 2019; 145(12):04019154.

[5] Lan X, Chan TM and Young B. Structural behaviour and design of chord plastification in high strength steel CHS X-joints. Construction and Building Materials 2018;191:1252-1267.

[6] Lan X, Chan TM and Young B. Structural behaviour and design of high strength steel RHS X-joints. Engineering Structures 2019;200:109494.

[7] Lan X, Chan TM and Young B. Experimental study on the behaviour and strength of high strength steel CHS T-and X-joints. Engineering Structures 2020;206:110182.

[8] Pandey M and Young B. Post-Fire Behaviour of Cold-Formed High Strength Steel Tubular T-and X-Joints, Journal of Constructional Steel Research 2021;186:106859.

[9] Pandey M and Young B. Ultimate Resistances of Member-Rotated Cold-Formed High Strength Steel Tubular T-Joints under Compression Loads, Engineering Structures 2021;244:112601.

[10] Pandey M and Young B. Effect of Member Orientation on the Static Strengths of Cold-Formed High Strength Steel Tubular X-Joints, Thin-walled Structures 2022;170:108501.

[11] Pandey M and Young B. Stress Concentration Factors of Cold-Formed High Strength Steel Tubular T-Joints, Thin-walled Structures 2021;166:107996.

[12] Pandey M and Young B. Experimental Investigation on Stress Concentration Factors of Cold-formed High Strength Steel Tubular X-Joints, Engineering Structures 2021;243:112408.

[13] M. Feldmann, N. Schillo, S. Schaffrath, K. Virdi, T. Björk, N. Tuominen, M. Veljkovic, M. Pavlovic, P. Manoleas, M. Heinisuo, K. Mela, P. Ongelin, I. Valkonen, J. Minkkinen, J. Erkkilä, E. Pétursson, M. Clarin, A. Seyr, L. Horváth, B. Kövesdi, P. Turán, B. Somodi, Rules on High Strength Steel, Publications Office of the European Union, Luxembourg, 2016.

[14] X.Y. Lan, J. Wardenier and J.A. Packer. Performance and design of full-width RHS X and T joints under brace axial tension and brace bending. Thin-Walled Structures 2022 (in press).

[15] N. Tuominen and T. Björk, Capacity of RHS-Joints Made of High Strength Steels, CIDECT Report 5BZ, Lappeenranta University of Technology, Finland, 2016.

[16] X.Y. Lan, T.M. Chan, B. Young, Testing, finite element analysis and design of high strength steel RHS T-joints, Eng. Struct. 227 (2020) 111184.

[17] X.Y. Lan, T.M. Chan, B. Young, Structural behaviour and design of high strength steel CHS T-joints, Thin-Walled Struct. 159 (2021) 107215.

[18] A. Takahashi and M. Iino. ISIJ Int. 36 (1996) 241-245.

[19] N.N. Jia, K. Guo, Y.M. He, Y.H. Wang, J.G. Paneg, T.S. Wang, Mater. Sci. Eng. A. 700 (2017) 175-182.

[20] Y. Ju, A. Goodall, M. Strangwood, C. Davis, Mater. Sci. A. 738 (2018) 174-189.

[21] Shikanai N., Mitao S., and Endo S. Recent development in microstructural control technologies through the thermo-mechanical control process (TMCP) with JFE steel's high-performance plates. JFE technical report, 2008, 11(6), 1-6.

[22] ANSI/AISC 360. Specification for Structural Steel Buildings. American Institution of Steel Construction, Chicago, USA; 2016.

[23] BS ISO 14346. Static design procedure for welded hollow-section joints – Recommendations. British Standard International Standards, Geneva, Switzerland; 2013.
[24] Eurocode 3 (EC3), Design of Steel Structures-Part 1-8: Design of Joints, EN 1993-1-8, European Committee for Standardization, CEN, Brussels, Belgium, 2005.
[25] IIW Doc. XV-1402-12 and IIW Doc. XV-E-12-433. Static design procedure for welded hollow section joints – Recommendations. International Institute of Welding, Paris, France, 2012.
[26] Packer JA, Wardenier J, Zhao XL, Vegte GJ van der, Kurobane Y. Design guide for rectangular hollow section (RHS) joints under predominantly static loading. Comite´ International pour le Developpement et l'Etude de la Construction TuECbulaire (CIDECT), Design Guide No. 3, 2nd edn., LSS Verlag, Dortmund, Germany, 2009.
[27] Eurocode 3 (EC3), Design of steel structures. Part 1-12: Additional rules for the extension of EN 1993 up to steel grades S700, EN 1993-1-12, European Committee for Standardization, CEN, Brussels, Belgium, 2007.
[28] Pandey M and Young B. Structural performance of cold-formed high strength steel tubular X-Joints under brace axial compression. Engineering Structures, 2020; 208:109768.
[29] Pandey M and Young B. Static resistances of cold-formed high strength steel tubular non-90° X-Joints. Engineering Structures 2021;239:112064.
[30] Pandey M, Young B. Tests of cold-formed high strength steel tubular T-joints. Thin-Walled Struct 2019;143:106200.
[31] Pandey M, Young B. Compression capacities of cold-formed high strength steel tubular T-joints. J Constr Steel Res 2019;162:105650.
[32] Feng R., Wu C., Chen Z., Roy K., Chen B. and Lim J. B. An experimental study on stainless steel hybrid tubular joints with square braces and circular chord. Thin-Walled Structures, 2020, 155, 106919.
[33] Abaqus/Standard. Version 6.17. USA: K. a. S. Hibbit; 2017.
[34] Crockett P. Finite element analysis of welded tubular connections. PhD Thesis, University of Nottingham, 1994.
[35] Pandey M, Chung KF and Young B. Design of cold-formed high strength steel tubular T-joints under compression loads. Thin-Walled Structures 2021;164:107573.
[36] Pandey M, Chung KF and Young B. Numerical investigation and design of fully chord supported tubular T-joints. Engineering Structures 2021;239:112063.
[37] Li HT and Young B. Cold-formed stainless steel RHS members undergoing combined bending and web crippling: Testing, modelling and design. Engineering Structures 2022;250:113466.
[38] Li HT and Young B. Cold-formed high-strength steel tubular structural members under combined bending and bearing. ASCE Journal of Structural Engineering 2019;145(8):04019081.
[39] Feng R., Wu C., Chen Z., Roy K., Chen B. and Lim J. B. Finite element modelling and proposed design rules of stainless steel hybrid tubular joints with square braces and circular chord. Journal of Constructional Steel Research, 2021, 179, 106557.
[40] Stroetmann R, Kastner T, Halsig A and Mayr P. Mechanical properties and a new design approach for welded joints at high strength steels. Hong Kong:Engineering Research and Practice for Steel Construction; 2018:79–90.
[41] Javidan F, Heidarpour A, Zhao XL, Hutchinson CR and Minkkinen J. Effect of weld on the mechanical properties of high strength and ultra-high strength steel tubes in fabricated hybrid sections. Eng Struct 2016;118:16–27.
[42] Amraei M., Ahola A., Afkhami S., Bjork T., Heidarpour A. and Zhao X.L. .Effects of heat input on the mechanical properties of butt-welded high and ultra-high strength steels, Engineering

Structures, 2019, 198, 109460.
[43] Amraei M., Afkhami S., Javaheri V., Larkiola J., Skriko T., Bjork T. and Zhao X.L. .Mechanical properties and microstructural evaluation of the heat-affected zone in ultra-high strength steels, Thin-Walled Structures, 2020, 157, 107072.
[44] Garifullin M, Bronzova MK, Heinisuo M, Mela K and Pajunen S. Cold-formed RHS T joints with initial geometrical imperfections. Magazine of Civil Engineering 2018,82(6).
[45] prEN 10219-2. Cold formed welded structural hollow sections of non-alloy and fine grain steels-Part 2: Tolerances, dimensions and sectional properties. European Committee for Standardization (CEN), Brussels, Belgium; 2006.
[46] SSAB. Strenx Tube 900 MH. Data Sheet 2042, Sweden, 2017.
[47] SSAB. Strenx Tube 960 MH. Data Sheet 2043, Sweden, 2017.
[48] AWS D1.1/D1.1M, Structural Welding Code – Steel, American Welding Society (AWS), Miami, USA, 2020.
[49] AISI S100. North American Specification for the design of cold-formed steel structural members. American Iron and Steel Institute (AISI), Washington, D.C., USA, 2016.
[50] Cai WY, Wang YB, Li GQ and Stroetmann R. Comparative study on strength of TMCP and QT high-strength steel butt-welded joints. Journal of Constructional Steel Research, 2022, 197, 107447.
[51] Lan X, Wardenier J and Packer JA. Design of chord sidewall failure in RHS joints using steel grades up to S960. Thin-Walled Structures 2021;163:107605.
[52] J.A. Packer, Web crippling of rectangular hollow sections, J. Struct. Eng. 110 (10) (1984) 2357–2373.
[53] J. Becque, S. Cheng, Sidewall buckling of equal-width RHS truss X-joints, J. Struct. Eng. 143 (2) (2016) 04016179.
[54] J. Becque, and T. Wilkinson. Experimental investigation of the static capacity of grade C450 RHS T and X truss joints. 14th Tubular Structures, CRC Press, London, 2012.
[55] J. Kuhn, J.A. Packer, Y.J. Fan, RHS webs under transverse compression, Can. J. Civil Eng. 46 (9) (2019) 810–827.
[56] J. Wardenier, X.Y. Lan, J.A. Packer, Evaluation of Design Methods for Chord Sidewall Failure in RHS Joints using Steel Grades Up to S960 – State of the Art, IIW Doc. XV-E-489-20, 2020.
[57] J. Becque, T. Wilkinson, The capacity of grade C450 cold-formed rectangular hollow section T and X connections: an experimental investigation, J. Constr. Steel Res. 133 (2017) 345–359.
[58] T. Björk, H. Saastamoinen, Capacity of CFRHS X joints made of double grade S420 steel, in: Proceedings of 14th International Symposium on Tubular Structures, London, U.K, 2012.
[59] EN 1993-1-1, Eurocode 3: Design of Steel Structures–Part 1-1: General Rules and Rules for Buildings, European Committee for Standardization (CEN), Brussels, Belgium, 2005.

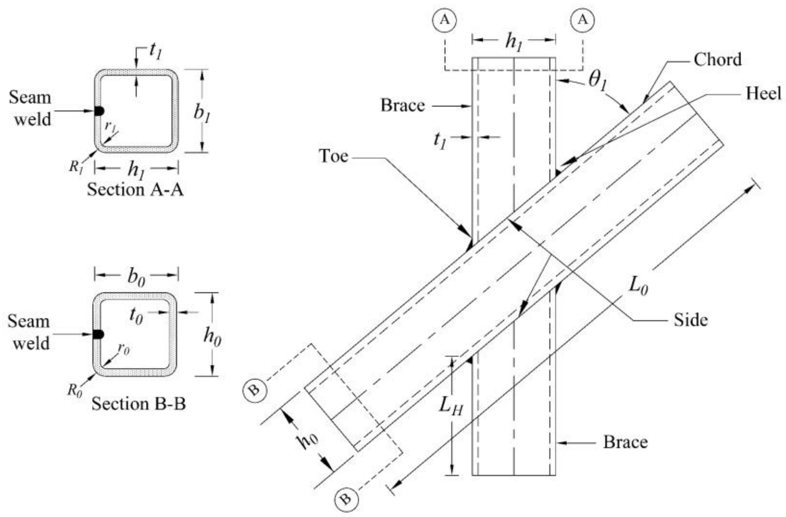

Fig. 1. Definitions of notations for RHS X-joint.

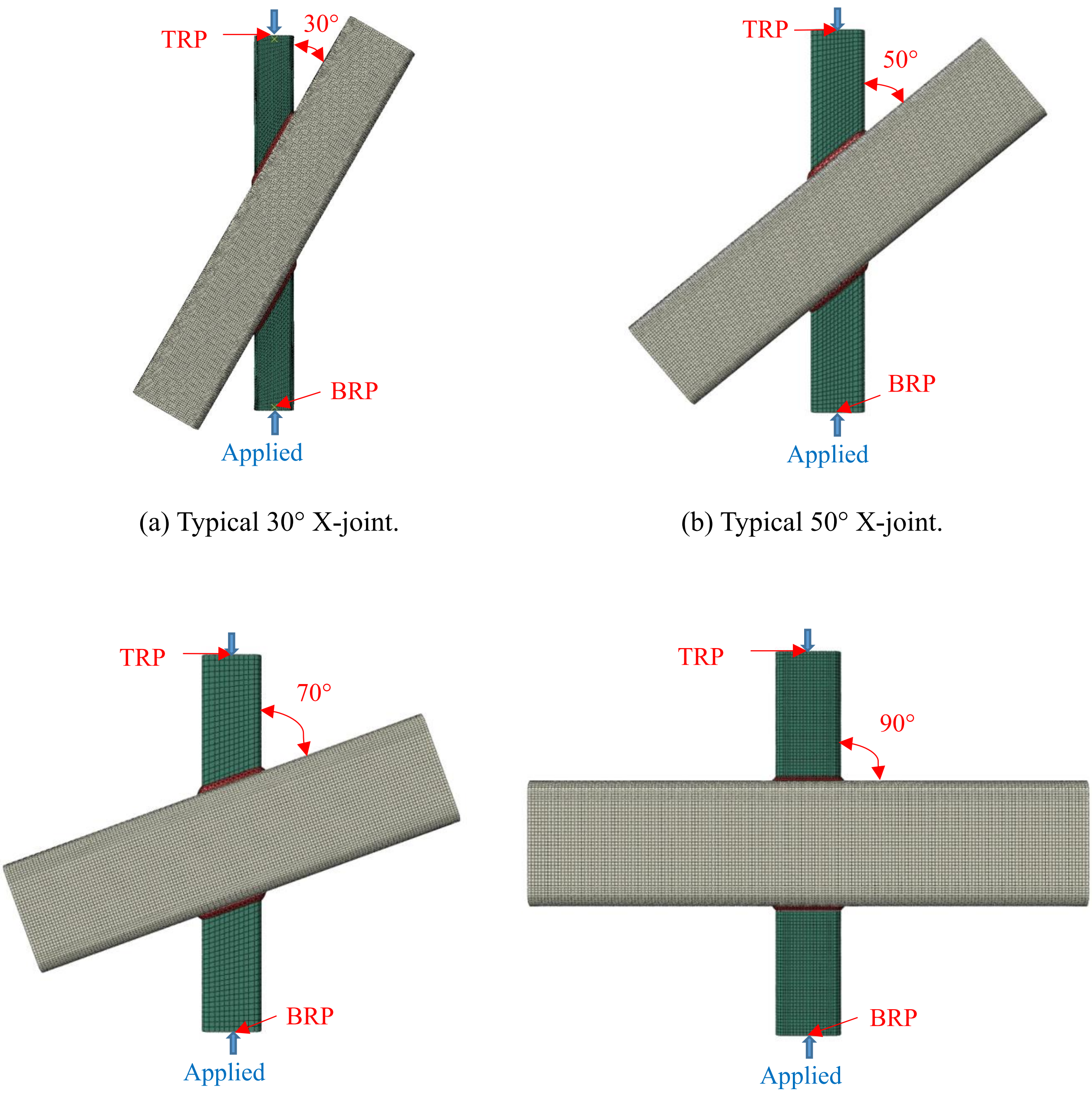

(a) Typical 30° X-joint.

(b) Typical 50° X-joint.

(c) Typical 70° X-joint.

(d) Typical 90° X-joint.

Fig. 2. Typical FE models of RHS X-joints.

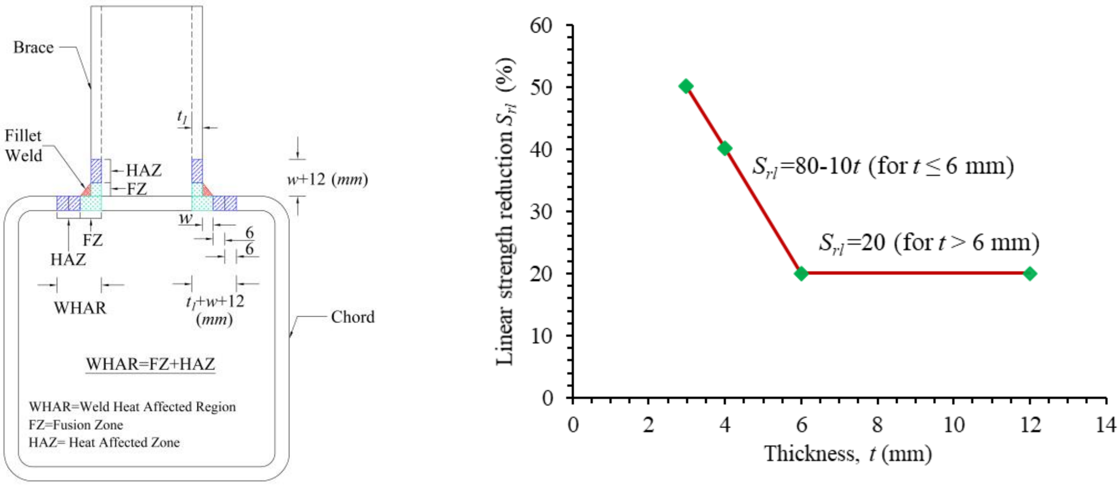

(a) Definition of WHAR.

(b) Linear strength reduction model.

Fig. 3. Weld heat affected region and linear strength reduction model [35].

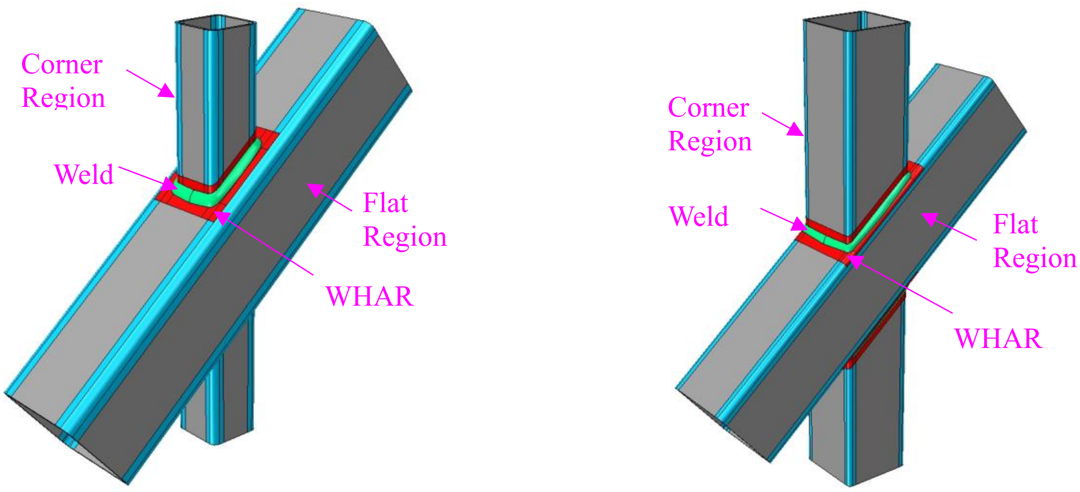

(a) WHAR spread when weld lies on flat region of chord.

(b) WHAR spread when weld lies on flat and corner regions of chord.

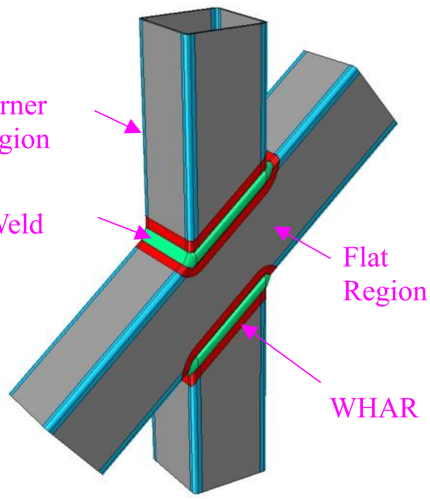

(c) WHAR spread for equal-width (β=1.0) RHS X-joints.

Fig. 4. Spread of weld heat affected region (WHAR) in typical RHS X-joints.

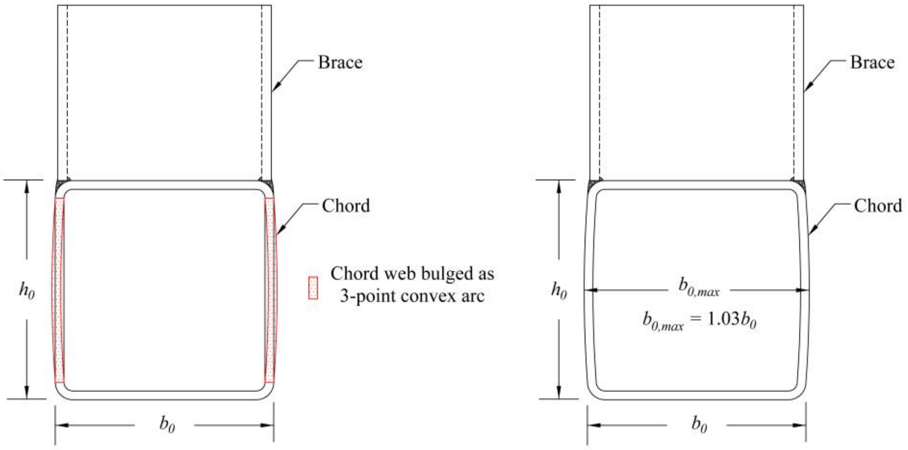

Fig. 5. Modelling of initial imperfection in chord webs of equal-width (β=1.0) RHS X-joints.

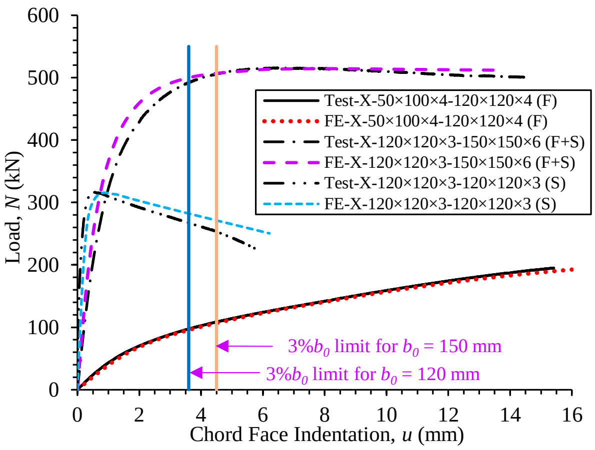

(a) Load vs chord face indentation curves.

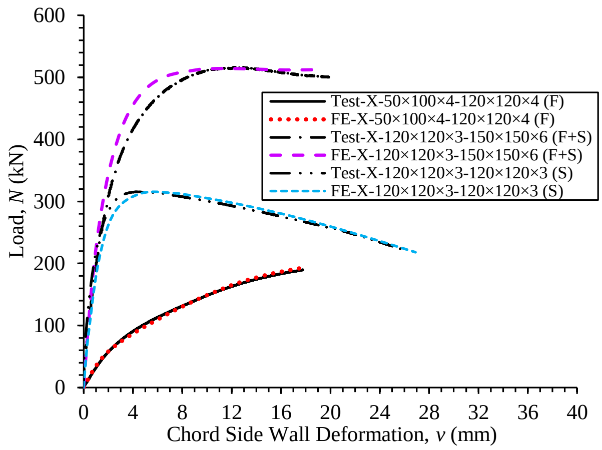

(b) Load vs chord side wall deformation curves.

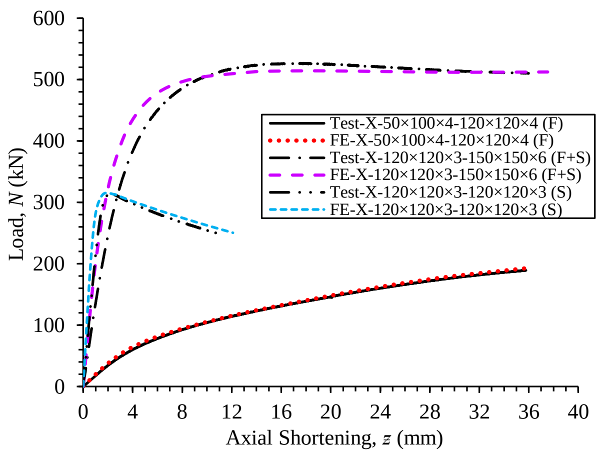

(c) Load vs axial shortening curves.

Fig. 6. Test vs FE load-deformation curves for 90° RHS X-joints.

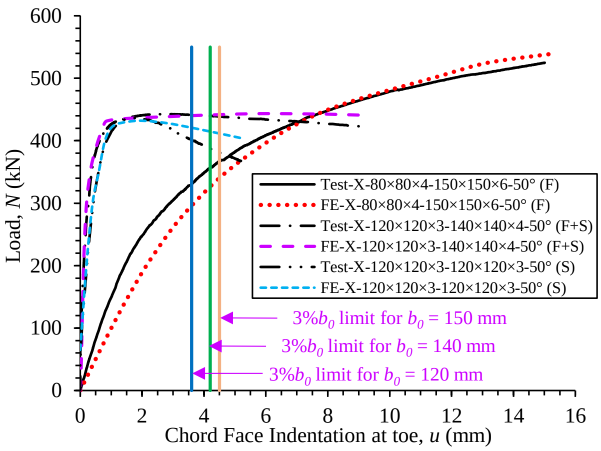

(a) Load vs chord face indentation curves.

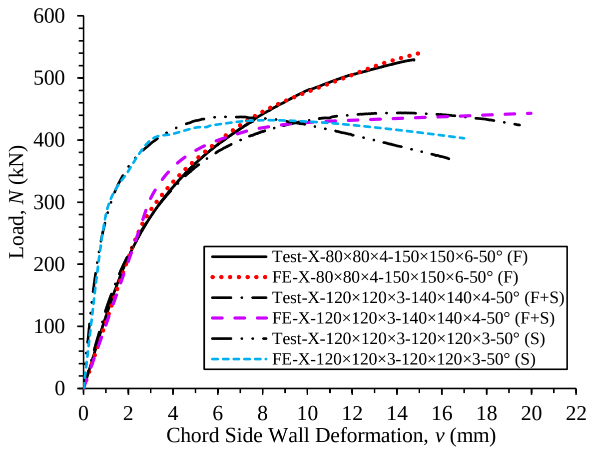

(b) Load vs chord side wall deformation curves.

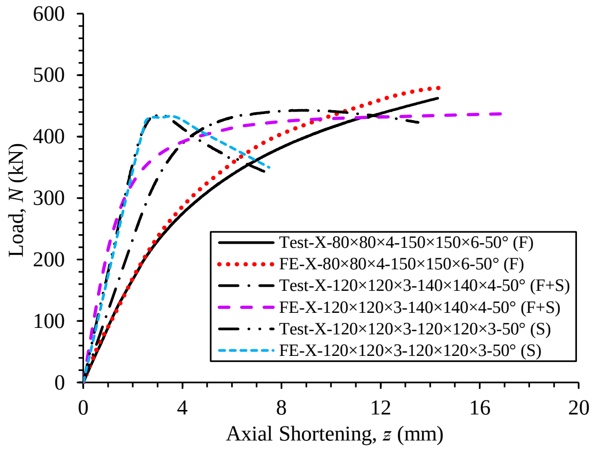

(c) Load vs axial shortening curves.

Fig. 7. Test vs FE load-deformation curves for non-90° RHS X-joints.

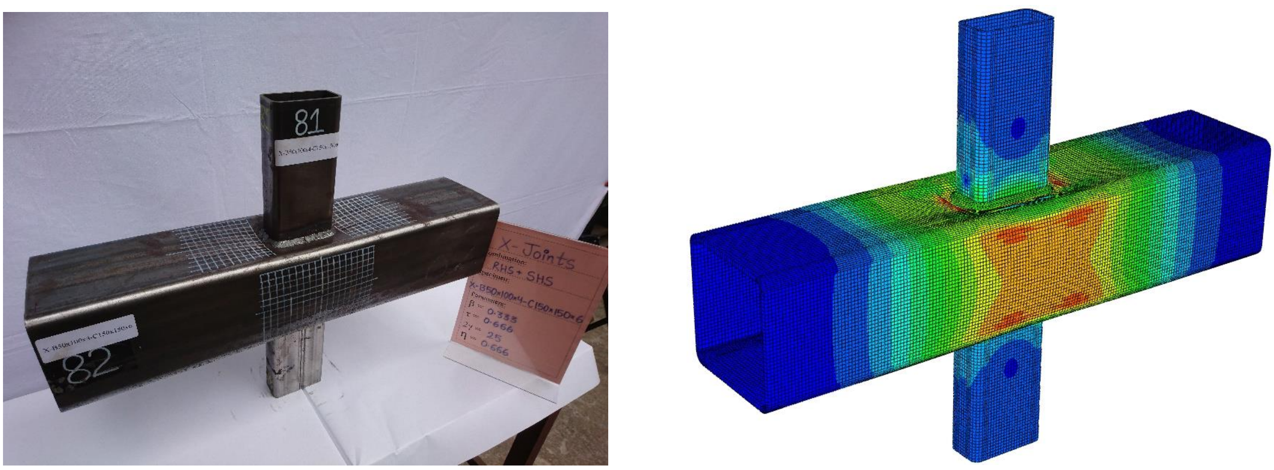

(a) Test vs FE comparison for chord face failure (F) mode of 90° RHS X-joints.

(b) Test vs FE comparison for combined failure (F+S) mode of 90° RHS X-joints.

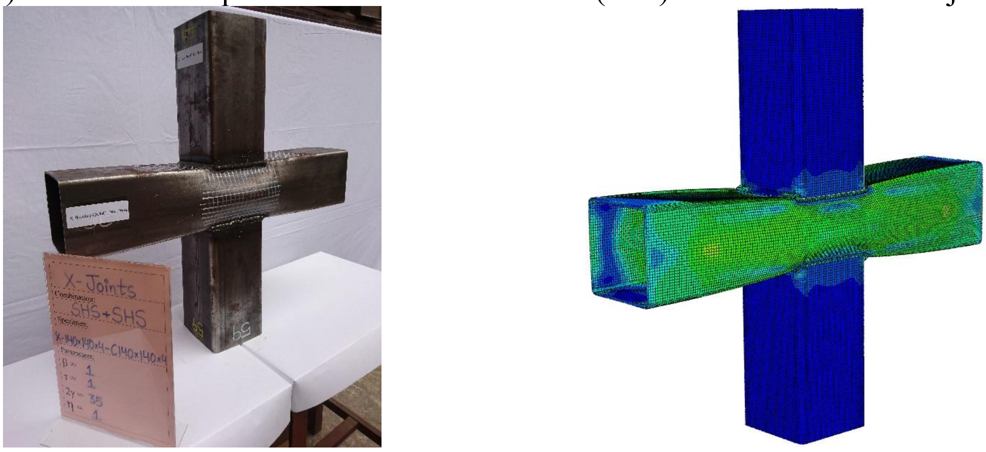

(c) Test vs FE comparison for chord side wall failure (S) mode of 90° RHS X-joints.

Fig. 8. Test vs FE failure mode comparisons for 90° RHS X-joints.

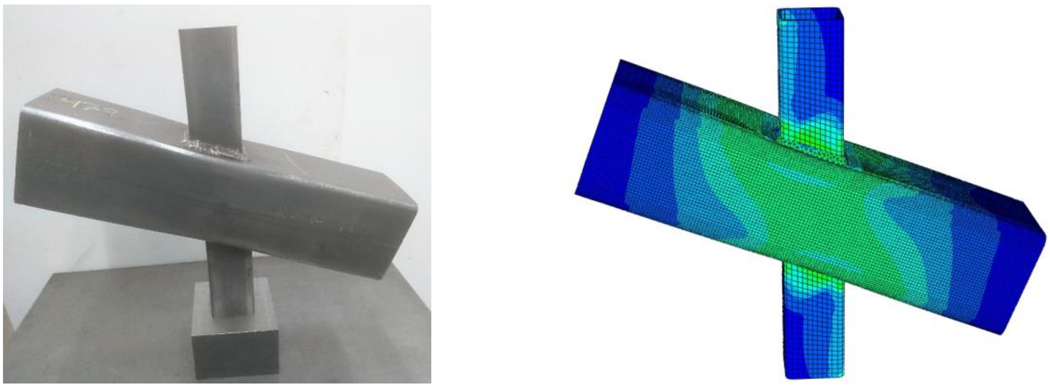

(a) Test vs FE comparison for chord face failure (F) mode of non-90° RHS X-joints.

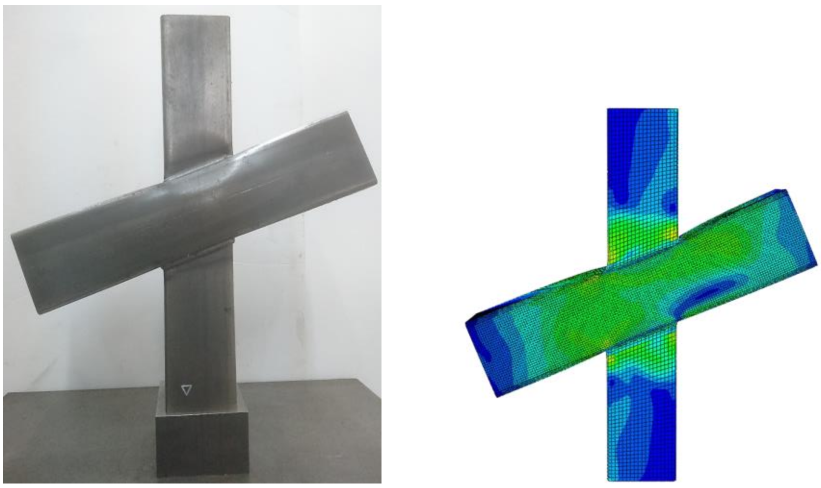

(b) Test vs FE comparison for combined failure (F+S) mode of non-90° RHS X-joints.

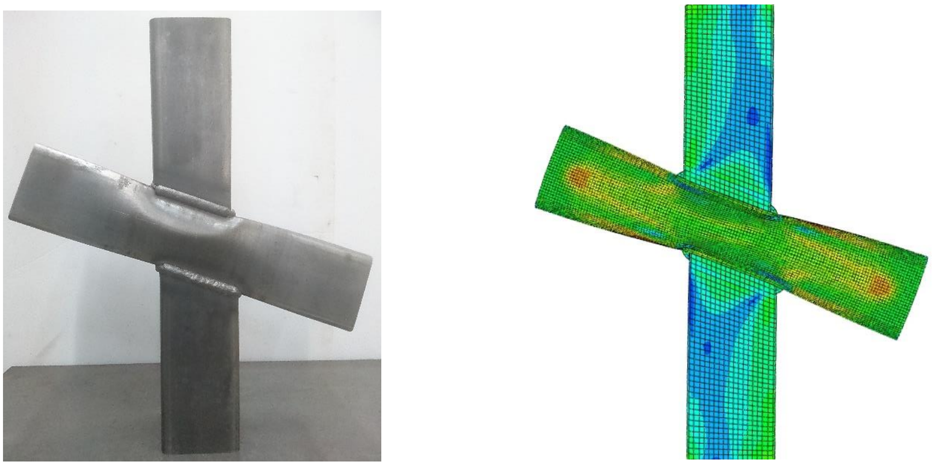

(c) Test vs FE comparison for chord side wall failure (S) mode of non-90° RHS X-joints.

Fig. 9. Test vs FE failure modes comparisons for non-90° RHS X-joints.

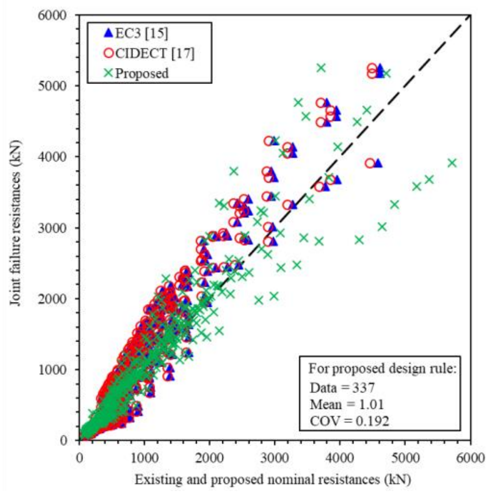

Fig. 10. Comparisons of test and FE joint failure resistances with current and proposed nominal resistances for chord face failure (F) mode.

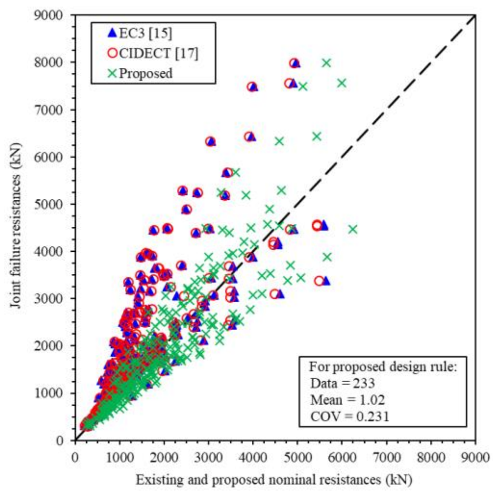

Fig. 11. Comparisons of test and FE joint failure resistances with current and proposed nominal resistances for combined failure (F+S) mode.

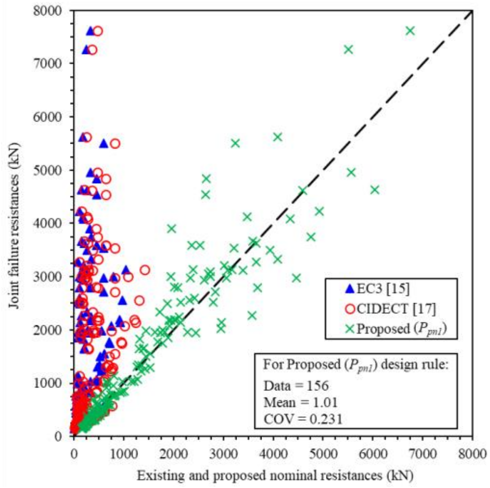

Fig. 12. Comparisons of test and FE joint failure resistances with current and proposed nominal resistances for chord side wall failure (S) mode.

Table 1. Test vs FE joint failure resistance comparisons for 90° RHS X-joints.

Specimens X-$b_1 \times h_1 \times t_1$-$b_0 \times h_0 \times t_0$	β	Failure modes	Test Resistances[#] (kN) N_f	FE Resistances (kN) N_{FE}	$\frac{N_f}{N_{FE}}$
X-50×100×4-150×150×6	0.34	F	160.3	157.8	1.02
X-50×100×4-150×150×6-R	0.34	F	165.3	158.2	1.05
X-50×100×4-140×140×4	0.36	F	71.9	68.2	1.05
X-50×100×4-120×120×4	0.42	F	97.9	95.9	1.02
X-60×100×4-120×60×4	0.50	F	146.6	144.5	1.01
X-80×80×4-150×150×6	0.53	F	239.4	237.3	1.01
X-80×80×4-140×140×4	0.57	F	111.6	109.8	1.02
X-80×80×4-120×120×4	0.66	F	173.9	174.1	1.00
X-80×80×4-120×120×3	0.67	F	101.2	102.1	0.99
X-100×50×4-140×140×4	0.72	F	147.2	149.3	0.99
X-80×80×4-100×50×4	0.80	F+S	319.5	313.8	1.02
X-120×120×4-150×150×6	0.81	F+S	556.2	561.1	0.99
X-120×120×4-150×150×6-R	0.81	F+S	559.8	560.9	1.00
X-120×120×3-150×150×6	0.80	F+S	506.3	505.9	1.00
X-100×60×4-120×120×6	0.82	F+S	524.0	519.5	1.01
X-100×100×4-120×60×4	0.84	F+S	359.3	358.2	1.00
X-120×120×3-140×140×4	0.86	F+S	310.8	313.1	0.99
X-120×120×4-140×140×4	0.87	F+S	350.3	351.9	1.00
X-100×50×4-100×50×4	1.00	S	482.2	479.5	1.01
X-80×80×4-80×80×4	1.00	S	594.5	589.3	1.01
X-120×120×4-120×120×4	1.00	S	566.8	566.5	1.00
X-140×140×4-140×140×4	1.00	S	483.6	478.9	1.01
X-120×120×3-120×120×3	1.00	S	316.8	313.2	1.01
X-120×120×4-120×120×3	1.00	S	317.8	312.8	1.02
				Mean (P_m)	1.01
				COV (V_p)	0.016

Note: [#] Data obtained from Pandey and Young [28]; F = Chord face failure; F+S = Combined failure; S = Chord side wall failure.

Table 2. Test vs FE joint failure resistance comparisons for non-90° RHS X-joints.

Specimens X-b_1×h_1×t_1-b_0×h_0×t_0-θ_1	β	Failure modes	Test Resistances[#] (kN) N_f	FE Resistances (kN) N_{FE}	$\frac{N_f}{N_{FE}}$
X-80×80×4-150×150×6-30°	0.53	F	685.7	692.3	0.99
X-100×100×4-120×60×4-30°	0.84	F+S	765.6	760.1	1.01
X-100×100×4-120×60×4-30°-R	0.84	F+S	791.3	763.3	1.04
X-120×120×3-140×140×4-30°	0.86	F+S	777.4	759.9	1.02
X-120×120×3-120×120×3-30°	1.00	S	690.8	702.1	0.98
X-120×120×4-120×120×4-30°	1.00	S	1036.9	1034.3	1.00
X-80×80×4-150×150×6-50°	0.53	F	367.3	342.3	1.07
X-120×120×3-150×150×6-50°	0.80	F+S	722.0	719.2	1.00
X-100×100×4-120×60×4-50°	0.84	F+S	475.0	478.5	0.99
X-120×120×3-140×140×4-50°	0.86	F+S	442.6	443.5	1.00
X-120×120×3-120×120×3-50°	1.00	S	436.7	431.8	1.01
X-120×120×4-120×120×4-50°	1.00	S	763.3	766.1	1.00
X-80×80×4-150×150×6-70°	0.53	F	335.6	327.2	1.03
X-120×120×3-150×150×6-70°	0.80	F+S	571.2	575.1	0.99
X-100×100×4-120×60×4-70°	0.84	F+S	403.3	398.0	1.01
X-120×120×3-140×140×4-70°	0.86	F+S	356.8	359.1	0.99
X-120×120×3-120×120×3-70°	1.00	S	348.0	345.4	1.01
X-120×120×4-120×120×4-70°	1.00	S	613.1	612.0	1.00
				Mean (P_m)	1.01
				COV (V_p)	0.021

Note: [#] Data obtained from Pandey and Young [29]; F = Chord face failure; F+S = Combined failure; S = Chord side wall failure.

Table 3. Comparison summary for X-joints failed by chord face failure mode (0.30≤β≤0.75).

θ_1	Parameters	Comparisons				
		$\frac{N_f}{N_{E,X}^*}$	$\frac{N_f}{N_{E,X}}$	$\frac{N_f}{N_{C,X}^*}$	$\frac{N_f}{N_{C,X}}$	$\frac{N_f}{N_{pn}}$
30°	No. of data (n)	82	82	82	82	82
	Mean (P_m)	0.90	1.12	1.04	1.15	1.06
	COV (V_p)	0.214	0.214	0.214	0.214	0.212
50°	No. of data (n)	82	82	82	82	82
	Mean (P_m)	0.93	1.16	1.07	1.19	1.00
	COV (V_p)	0.326	0.326	0.326	0.326	0.199
70°	No. of data (n)	82	82	82	82	82
	Mean (P_m)	0.93	1.16	1.07	1.19	1.00
	COV (V_p)	0.333	0.333	0.333	0.333	0.170
90°	No. of data (n)	91	91	91	91	91
	Mean (P_m)	0.92	1.15	1.06	1.17	0.98
	COV (V_p)	0.319	0.319	0.320	0.320	0.176
Overall	No. of data (n)	337	337	337	337	337
	Mean (P_m)	0.92	1.15	1.06	1.18	1.01
	COV (V_p)	0.302	0.302	0.303	0.303	0.192
	Resistance factor (ϕ)	1.00	1.00	1.00	1.00	0.75
	Reliability index (β_0)	0.99	1.55	1.45	1.72	2.55

Table 4. Comparison summary for X-joints failed by combined failure mode (0.80≤β≤0.90).

θ_1	Parameters	Comparisons				
		$\frac{N_f}{N_{E,X}^*}$	$\frac{N_f}{N_{E,X}}$	$\frac{N_f}{N_{C,X}^*}$	$\frac{N_f}{N_{C,X}}$	$\frac{N_f}{N_{pn}}$
30°	No. of data (n)	56	56	56	56	56
	Mean (P_m)	0.93	1.16	1.05	1.17	1.10
	COV (V_p)	0.340	0.340	0.328	0.328	0.257
50°	No. of data (n)	57	57	57	57	57
	Mean (P_m)	1.18	1.47	1.32	1.46	0.93
	COV (V_p)	0.324	0.324	0.305	0.305	0.230
70°	No. of data (n)	57	57	57	57	57
	Mean (P_m)	1.29	1.62	1.44	1.60	1.05
	COV (V_p)	0.347	0.347	0.332	0.332	0.228
90°	No. of data (n)	62	62	62	62	62
	Mean (P_m)	1.11	1.38	1.23	1.37	1.01
	COV (V_p)	0.209	0.209	0.194	0.194	0.165
Overall	No. of data (n)	233	233	233	233	233
	Mean (P_m)	1.13	1.41	1.26	1.40	1.02
	COV (V_p)	0.330	0.330	0.314	0.314	0.231
	Resistance factor (ϕ)	1.00	1.00	1.00	1.00	0.70
	Reliability index (β_0)	1.42	1.96	1.84	2.10	2.61

Table 5. Summary of comparisons between test and FE ultimate capacities with existing and proposed nominal joint resistances for X-joints failed by chord side wall failure mode (β=1.0).

θ_1	Parameters	Comparisons					
		$\frac{N_f}{N_{E,X}^*}$	$\frac{N_f}{N_{E,X}}$	$\frac{N_f}{N_{C,X}^*}$	$\frac{N_f}{N_{C,X}}$	$\frac{N_f}{N_{pn1}}$	$\frac{N_f}{N_{pn2}}$
30°	No. of data (n)	38	38	38	38	38	38
	Mean (P_m)	9.97	12.46	8.05	8.94	1.20	0.97
	COV (V_p)	0.855	0.855	0.850	0.850	0.232	0.217
50°	No. of data (n)	38	38	38	38	38	38
	Mean (P_m)	7.36	9.20	5.96	6.63	0.96	1.01
	COV (V_p)	0.803	0.803	0.795	0.795	0.205	0.196
70°	No. of data (n)	38	38	38	38	38	38
	Mean (P_m)	6.12	7.65	4.97	5.52	0.91	1.02
	COV (V_p)	0.757	0.757	0.747	0.747	0.169	0.161
90°	No. of data (n)	42	42	42	42	42	42
	Mean (P_m)	5.50	6.88	4.48	4.97	0.97	1.03
	COV (V_p)	0.759	0.759	0.749	0.749	0.179	0.198
Overall	No. of data (n)	156	156	156	156	156	156
	Mean (P_m)	7.18	8.98	5.82	6.47	1.01	1.00
	COV (V_p)	0.862	0.862	0.854	0.854	0.231	0.195
	Resistance factor (ϕ)	0.80	0.80	0.80	0.80	0.70	0.75
	Reliability index (β_0)	2.94	3.19	2.78	2.90	2.57	2.51

Table 6. Values of coefficients for chord face failure unified design rule.

Joint Types	Coefficients					
	A	B	C	D	E	F
RHS-RHS X-Joint	28	7	-7	1	0.01	1.4
RHS-RHS T-Joint [35]	30	4.5	-6.6	0.5	0.03	0*
RHS-RHS TF-Joint [36]	28	6.5	-7	0.7	0.018	0*

Note: * Non-90° T- and TF-joints were not investigated in Pandey et al. [35,36].

Table 7. Values of coefficients for combined failure unified design rule.

Joint Types	Coefficients					
	A	B	C	D	E	F
RHS-RHS X-Joint	60	8	-38	0.9	0.003	$0.04\theta_1$ - 0.1
RHS-RHS T-Joint [35]	55	4.5	-33	0.75	0.0075	0*
RHS-RHS TF-Joint [36]	65	12	-45	0.83	0.003	0*

Note: * Non-90° T- and TF-joints were not investigated in Pandey et al. [35,36].

Table 8. Values of coefficients for chord side wall failure unified design rule.

Joint Types	Coefficients						
	A	B	C	D	E	F	G
RHS-RHS X-Joint	1.4	-0.05	2.4	$2e^{-0.05\left(\frac{h_0}{t_0}\right)^{(1.1-0.001\theta_1)}}$	0.4	2	0.7
RHS-RHS T-Joint [35]	1.83	-0.05	1.2	$588\left(\frac{h_0}{t_0}\right)^{-2.17}$	1.5	1	0*
RHS-RHS TF-Joint [36]	1.1	-0.05	2.2	$2.5e^{-0.06\left(\frac{h_0}{t_0}\right)}$	0.67	1.7	0*

Note: * Non-90° T- and TF-joints were not investigated in Pandey et al. [35,36].